Volume 10
Number 6
June 2025
Pages 427–496

MSDE

Molecular Systems Design & Engineering

rsc.li/molecular-engineering

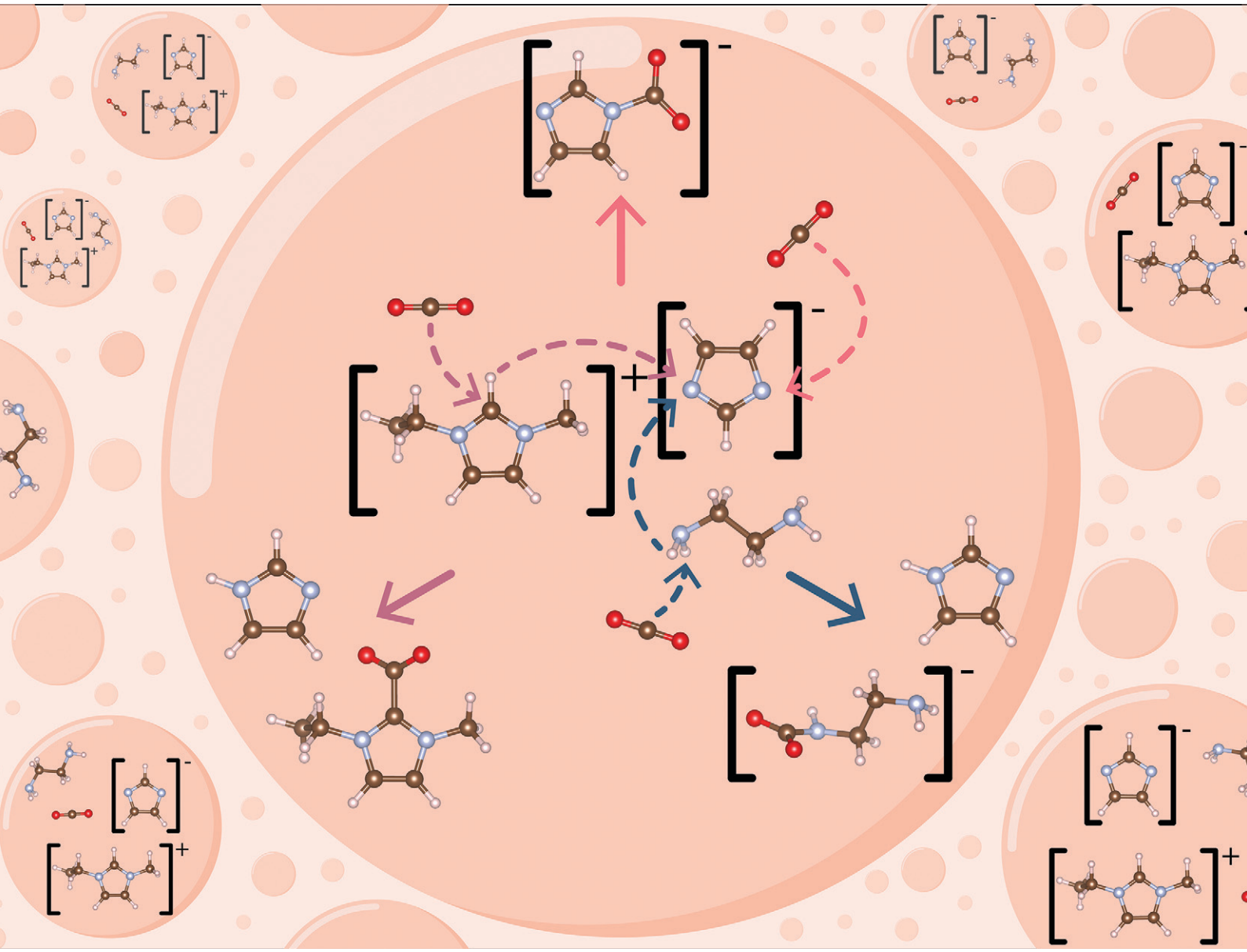

ISSN 2058-9689

ROYAL SOCIETY OF CHEMISTRY

PAPER

Stephen P. Vicchio, Rachel B. Getman *et al.*

Quantum chemical screening of eutectic solvent components for insights into CO_2 complexation mechanisms

IChemE ADVANCING CHEMICAL ENGINEERING WORLDWIDE

MSDE

PAPER

View Article Online
View Journal | View Issue

Cite this: *Mol. Syst. Des. Eng.*, 2025, **10**, 447

Quantum chemical screening of eutectic solvent components for insights into CO_2 complexation mechanisms†

Stephen P. Vicchio, *[a] Osasumwen J. Ikponmwosa [b] and Rachel B. Getman *[ab]

Developing new negative emission technologies (NETs) to capture atmospheric CO_2 is necessary to limit global temperature rise below 1.5 °C by 2050. The technologies, such as direct air capture (DAC), rely on sorption materials to harvest trace amounts of CO_2 from ambient air. Deep eutectic solvents (DESs) and eutectic solvents (ESs), a subset of ionic liquids (ILs), are all promising new CO_2 sorption materials for DAC. However, the experimental design space for different DESs/ESs/ILs is vast, with the exact CO_2 complexation pathways difficult to elucidate; this creates significant limitations in rationally designing new materials with targeted CO_2 sorption energetics. Herein, the CO_2 complexation pathways for a structural library of different DES/ES components are computed using quantum chemical calculations (*i.e.*, density functional theory). For the entire structure library, we report the energies of elementary CO_2 binding and proton transfer reactions as these reactions are fundamental in DAC within DESs and ESs. These elementary reactions are combined to generate CO_2 complexation pathways and calculate their free energies. The different elementary steps and reaction pathways demonstrate the range of CO_2 complexation free energies and the significance between CO_2 binding and proton transfer reactions. We also report the CO_2 complexation free energies with different functional groups around the CO_2 sorption site, supporting the concept of functionalization for tuning CO_2 complexation thermodynamics. Additionally, our findings suggest potential descriptors, such as proton affinity or pK_a, could be useful when identifying candidate species for ESs and predicting/rationalizing product distributions. Our work has implications for experimental synthesis, characterization, and performance evaluation of new DAC sorption materials.

Received 4th March 2025,
Accepted 30th April 2025

DOI: 10.1039/d5me00034c

rsc.li/molecular-engineering

Design, System, Application

The development of negative emission technologies (NETs) is crucial for mitigating global climate change by capturing atmospheric CO_2. Among these technologies, direct air capture (DAC) relies on advanced sorbent materials to efficiently harvest CO_2 from ambient air. Deep eutectic solvents (DESs) and eutectic solvents (ESs), as subsets of ionic liquids (ILs), show significant promise as CO_2 sorbents due to their unique properties, including negligible vapor pressures, high thermal stabilities, and chemical tunability. However, the vast experimental design space and complex CO_2 complexation pathways present challenges in rationally designing new materials with targeted CO_2 sorption energetics. In this work, we employ quantum chemical calculations, specifically density functional theory (DFT), to investigate the CO_2 complexation mechanisms within a structural library of DES/ES components. By computing the energies of elementary CO_2 binding and proton transfer reactions, we generate comprehensive CO_2 complexation pathways and calculate their free energies. This approach allows us to explore the impact of various functional groups on CO_2 binding thermodynamics, providing insights into the tunability of CO_2 sorption properties. Our findings highlight the potential of functionalization to enhance CO_2 complexation by modifying the chemical environment around the sorption site. Additionally, we identify potential descriptors, such as proton affinity or pK_a, that could aid in predicting and rationalizing CO_2 sorption performance. This work lays the groundwork for the experimental synthesis, characterization, and optimization of new DAC sorbent materials, ultimately contributing to the advancement of NETs and the global effort to combat climate change.

Introduction

Reducing CO_2 emissions from burning non-renewable fossil fuels is insufficient to remediate global climate change.[1] Therefore, the development of new negative emission technologies (NETs)[2–5] to remove previously emitted CO_2 is essential in limiting global temperature rise.[6] Direct air capture (DAC), one such NET, is a carbon capture process

[a] *Department of Chemical and Biomolecular Engineering, Clemson University, Clemson, South Carolina 29634-0909, USA. E-mail: stephen.vicchio@uky.edu*
[b] *William G. Lowrie Department of Chemical and Biomolecular Engineering, Ohio State University, Columbus, OH 43210, USA. E-mail: getman.11@osu.edu*
† Electronic supplementary information (ESI) available. See DOI: https://doi.org/10.1039/d5me00034c

that relies on novel sorbent materials to efficiently remove atmospheric CO_2 under ambient conditions.[6–9] Promising DAC materials include ionic liquids (ILs),[10–12] deep eutectic solvents (DESs),[10,13–15] metal–organic frameworks (MOFs),[16–20] and covalent organic frameworks (COFs).[21–23] These solid- and liquid-sorbent materials exhibit promising physical and chemical properties for DAC and are tunable. For state-of-the-art DAC materials,[24] higher gravimetric CO_2 uptake is achieved when CO_2 binds chemically (*e.g.*, ILs[25]) instead of physically (*e.g.*, MOFs[26]). This is particularly important for DAC, where the amount of CO_2 is very small. For DAC, there is a need to develop new materials that exhibit high CO_2 capacities, which requires a deeper understanding of the structure–function relationships that govern the CO_2 sorption process.

Both ILs and DESs are promising liquid sorbents for DAC due to their negligible vapor pressures, high thermal stabilities, and chemical tunabilities.[27–30] ILs are liquid salts comprising of both cationic and anionic components (charges of ±1) that melt below 100 °C.[31] Both these cationic and anionic components are hydrogen bond acceptors (HBAs). Examples of cationic components (*i.e.*, $[HBAc]^+$) are 1-ethyl-3-alkylimidazolium ($[EMIM]^+$) and choline ($[Ch]^+$), and examples of anionic components (*i.e.*, $[HBAa]^-$) are imidazolide ($[Im]^-$) and pyrrolide ($[Pyr]^-$).[32] DESs are similar to ILs in that they contain the cationic and anionic components, but DESs also contain a hydrogen bond donor (HBD), such as ethylene glycol (EG) that contributes to further melting point suppression[33,34] and, generally, lowers the viscosity of the solvent.[14,35] However, even eutectic solvents (ESs), where the exact 'deep' eutectic composition is not necessarily known, still exhibit promising properties for DAC.

The CO_2 uptake performance for ILs and DESs/ESs has been previously studied using experimental and computational approaches.[11,36–46] For example, Lee *et al.* elucidated the different CO_2 binding pathways for an imidazolium $[HBAc]^+$ and pyrrolide $[HBAa]^-$ in the presence of ethylene glycol (EG), finding that CO_2 prefers to bind to the $[HBAc]^+$.[47] Further advancements by Klemm *et al.* demonstrate how the CO_2 uptake capacity can be tuned by converting amino acid-based ILs to ESs through the addition of EG.[14] Supplemental modeling insights demonstrate how the HBD alters the interactions within the solvent leading to a difference in uptake for the IL *vs.* the ES.

These studies motivate the need for research aimed at identifying the CO_2 complexation mechanisms associated with CO_2 uptake. Developing strategies to predict CO_2 uptake performance *a priori* is of critical importance due to the large experimental design space for these materials. There are multiple mechanisms for CO_2 complexation within an ES,[37,48] as defined by the CO_2 binding site (*i.e.*, to the $[HBAc]^+$, the $[HBAa]^-$, and/or the HBD species). The simplest mechanism is complexation to the $[HBAa]^-$, where CO_2 can bind directly to the species without the need for proton transfer to create the binding site. However, the $[HBAc]^+$ and the HBD species can also accept CO_2 following proton transfer to create a site for complexation.[14,38,49,50] The thermodynamics and kinetics behind these different complexation pathways are influenced by several properties, including the chemical nature of the various components of the sorbent material. Ultimately, the goal is to understand how to tune CO_2 complexation in ILs/DESs/ESs *via* chemical functionality.

Along these lines, in this work we combine high-throughput screening and density functional theory (DFT) calculations to probe CO_2 complexation by identifying the CO_2 binding locations and thermodynamics for CO_2 binding and proton transfer reaction steps. Quantifying the complexation thermodynamics of the various species within ILs and DESs/ESs is fundamental for rationally designing tunable CO_2 sorbent materials. We specifically focus on ESs by computing the CO_2 complexation thermodynamics for ~420 combinations of ESs (*i.e.*, unique cations, anions, and HBDs species). A library of hypothetical ESs provides information into the CO_2 complexation thermodynamics associated with different complexation pathways and the intermolecular proton transfers. Additionally, $[HBAa]^-$ functionalization is also systematically explored by varying the functional groups around the CO_2 binding site with electron-donating and electron-withdrawing groups. Overall, our work provides fundamental insights into the CO_2 sorption for ESs while laying the groundwork for rationally constructing solvents for CO_2 capture.

Methodology

The following sections discuss CO_2 complexation to the HBA and HBD components of ESs. For the HBA species, the cationic component is denoted as HBAc and the anionic component is denoted as HBAa. Charged species are denoted with brackets (*i.e.*, [ ]), and positive and negative charges are indicated using $[\ ]^+$ for cationic and $[\ ]^-$ and anionic species, respectively. Species without brackets are neutral. This delineation is essential when defining the different fundamental reactions since these reactions can involve proton transfers, which alter the charges of the species. For example, a proton transfer from the $[HBAc]^+$ or the HBD is needed before CO_2 complexation to those species. These proton transfers can neutralize or charge these species (*i.e.*, $[HBAc]^+ \rightarrow HBAcf + [H]^+$ or $HBD \rightarrow [HBD]^- + [H]^+$). Given the more favorable kinetics for intermolecular proton transfers over intramolecular proton transfers,[14,47,51] only intermolecular proton transfers are considered in this work. Protons that are transferred are hence transferred to the $[HBAa]^-$ (*i.e.*, $[HBAa]^- + [H]^+ \rightarrow HBAa$).

Structure library

A library of structures consisting of 5 $[HBAc]^+$, 12 $[HBAa]^-$, and 7 HBD species is investigated. Fig. 1 provides the full and abbreviated naming conventions and the structural representations for each species investigated, with the ball-

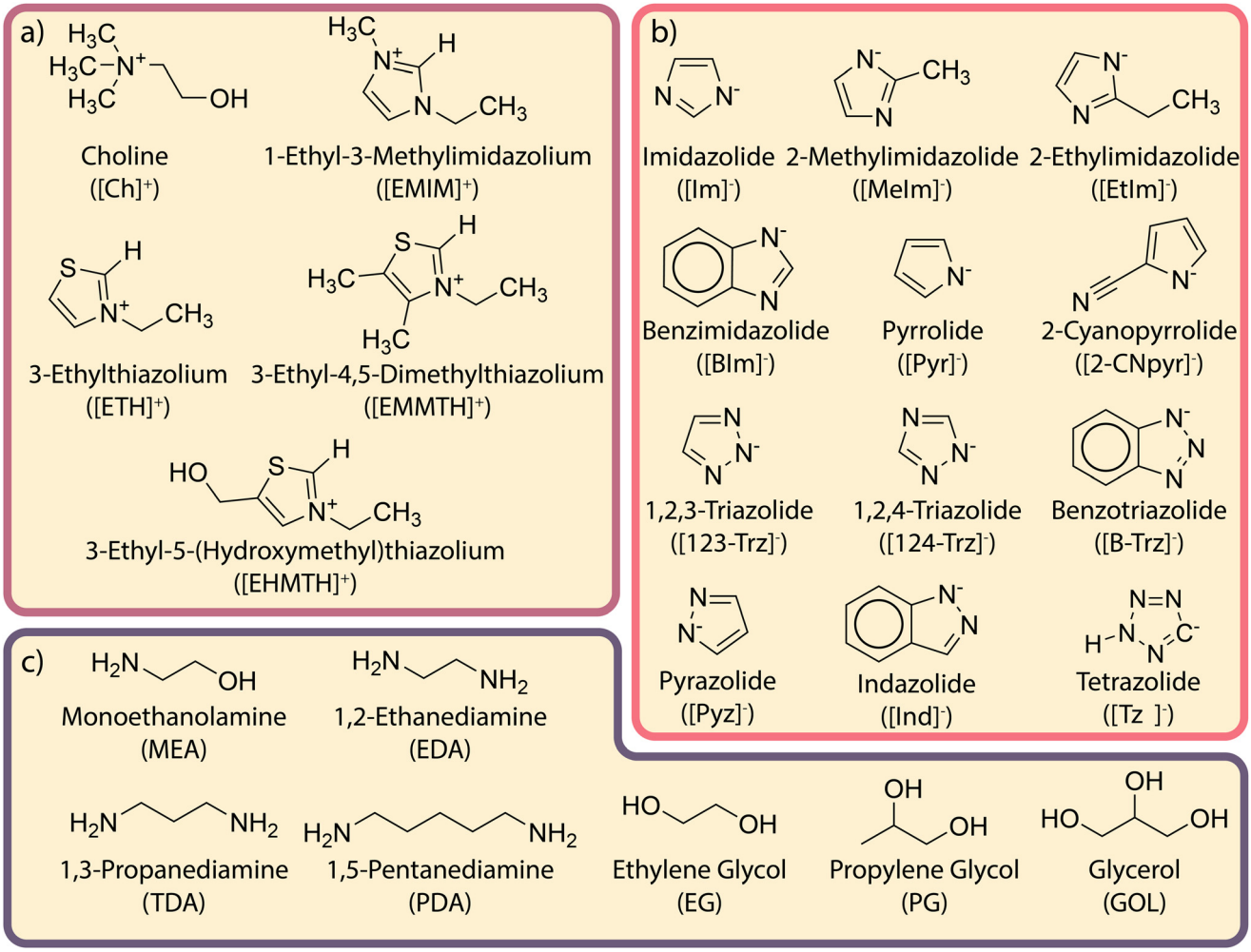

Fig. 1 The (a) hydrogen bond acceptor cations ($[HBAc]^+$), (b) hydrogen bond acceptor anions ($[HBAa]^-$), and (c) hydrogen bond donors (HBD) considered in this work. Both the full- and abbreviated-naming conventions are provided; the cationic and anionic species are identified with brackets and charges, respectively.

and-stick representations for all species provided in ESI† Section S1. Hypothetical ESs are constructed by combining a single $[HBAc]^+$, $[HBAa]^-$, and HBD species, producing a total of 420 different hypothetical mixtures. However, the total number of structures considered is even larger due to the multiple binding sites for CO_2 sorption and proton binding. For example, on a $[HBAa]^-$ comprising multiple N binding sites, CO_2 can bind to each N atom. All possible binding sites are considered to ensure the lowest energy conformer is found; the lowest energy conformers are reported in this manuscript. All structures are stored in an open, online repository.[52]

A subset of the $[HBAa]^-$ library (*i.e.*, $[Im]^-$ and $[Pyr]^-$) comprises similar species with different functional groups to investigate how different functional groups influence complexation. The functional groups are selected based on their electron-donating (*e.g.*, R–OH) and electron-withdrawing (*e.g.*, R–CHO) capabilities to understand the influence on CO_2 binding. The different functional groups are attached adjacent to the N binding site on the $[Im]^-$ and $[Pyr]^-$ species (Fig. 2a) at *ortho* positions relative to the CO_2 binding site. Specifically for $[Im]^-$, the functional group attachment occurs between the ring N atoms. These functionalized $[HBAa]^-$ species are compared to the unfunctionalized $[Im]^-$ and $[Pyr]^-$ species (which have a hydrogen atom in the *ortho* position). The left column in Fig. 2b shows the electron-donating groups (*i.e.*, R–Me, R–Et, R–OH, R–MeOH, and R–EtOH), and the right column in Fig. 2b shows the electron-withdrawing groups (R–F, R–CN, R–CHO, R–$COCH_3$, and R–$COOCH_3$) considered in this work.

Fundamental reactions

For a given $[HBAc]^+[HBAa]^-$:HBD ES, the hypothetical reaction mechanisms for CO_2 complexation, consisting of CO_2 binding and proton transfer steps, are presented in Table 1. The proton transfer reactions are included to account for cases where a species must donate a proton for CO_2 complexation. The generic, hypothetical reaction mechanisms determine the individual thermodynamics of

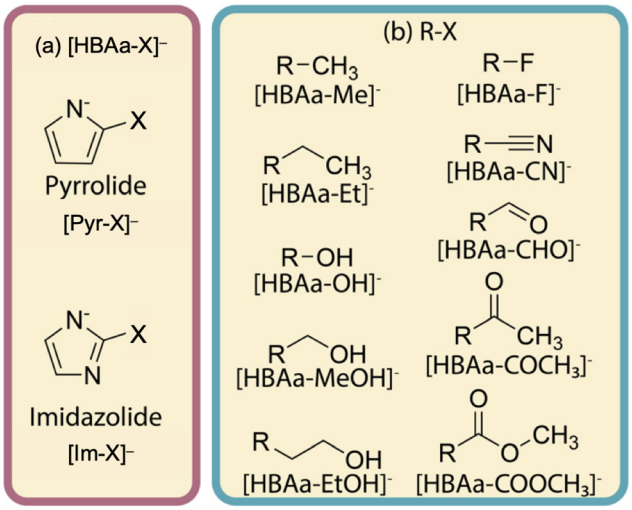

Fig. 2 [Pyr–X]⁻ and [Im–X]⁻ (a) were investigated for the influence of functionalization with the ten different functional groups (X) shown in (b). In part (b), electron-donating groups are shown in the left column while electron-withdrawing groups are shown in the right column.

Table 1 Fundamental reactions in a $[HBAc]^+[HBAa]^-$:HBD ES

Reaction mechanism	
$[HBAa]^- + [H]^+ \xrightarrow{\Delta G_1} HBAa$	R1
$[HBAa]^- + CO_2 \xrightarrow{\Delta G_2} [HBAa\text{–}CO_2]^-$	R2
$HBAc + [H]^+ \xrightarrow{\Delta G_3} [HBAc]^+$	R3
$HBAc + CO_2 \xrightarrow{\Delta G_4} [HBAc\text{–}CO_2]$	R4
$[HBD]^- + [H]^+ \xrightarrow{\Delta G_5} HBD$	R5
$[HBD]^- + CO_2 \xrightarrow{\Delta G_6} [HBD\text{–}CO_2]^-$	R6
$HBD + CO_2 \xrightarrow{\Delta G_7} HBD\text{–}CO_2$	R7
$[HBD\text{–}CO_2]^- + [H]^+ \xrightarrow{\Delta G_8} HBD\text{–}CO_2$	R8

All proton transfer reactions are written as affinity reactions for consistency.

each step and, when combined, the subsequent CO_2 complexation pathway free energies (Fig. 3).

Hypothetical reaction pathways

There are four distinct CO_2 complexation pathways considered in this work, which are outlined in Fig. 3. We label these pathways as the '$[HBAa]^-$', 'HBAc', '$[HBD]^-$', and 'HBD' pathways. The pathways are defined by the species that CO_2 binds to (*i.e.*, to the $[HBAa]^-$, HBAc, $[HBD]^-$, or HBD species). In the $[HBAa]^-$ pathway, CO_2 complexes directly to the $[HBAa]^-$ *via* reaction R2. CO_2 binding to the $[HBAc]^+$ requires proton transfer *via* the reverse of reaction R3 (all proton transfer reactions in Table 1 are written as affinity reactions for consistency) prior to complexation *via* reaction R4. CO_2 can complex to the HBD *via* two pathways. In the $[HBD]^-$ pathway, the HBD species first transfers a proton *via* the reverse of reaction R5. CO_2 then complexes to the deprotonated HBD species (*i.e.*, $[HBD]^-$) *via* reaction R6. An additional HBD pathway is considered where CO_2 first forms a weak complex with the neutral HBD molecule (reaction R7) prior to proton transfer *via* reaction R8. Theoretically, protons could be transferred to any negatively charged species in the solvent. We consider the case where they are transferred to the $[HBAa]^-$, converting it to the HBAa *via* reaction R1. The total free energy of complexation is denoted ΔG^c and is the sum of all necessary reactions *en route* to CO_2 complexation. For example, considering the $[HBAc]^+$ pathway (mauve color in Fig. 3), $\Delta G^c = -\Delta G_3 + \Delta G_1 + \Delta G_4$.

Quantum chemical (QM) calculations

The entire hypothetical reaction library is screened using the Gaussian16 Revision C.02 software,[53] with the structures, energies, and vibrational frequencies calculated at the B3LYP/6-311+G(d,p) level of theory. Test calculations performed at the ωB97XD/6-311+G(d,p) level of theory indicate a maximum 3.3 kJ mol^{-1} difference in free energy. Dispersion corrections formulated by Grimme *et al.* with Becke–Johnson (BJ) damping are included.[54,55] Solvation is needed to stabilize the electronic and geometric structures of the ionic species. We use implicit solvation for simplicity. However, explicit intermolecular interactions could contribute to the reported free energies. To learn how this could influence the results, we investigated the influence of hydrogen bonded HBD species on the $[HBAa]^-$ complexation pathway free energies. This analysis is summarized in ESI† Section S3. We find that, generally, explicit stabilization leads to a decrease in the CO_2 complexation free energies to the $[HBAa]^-$ species (*i.e.*, CO_2 complexation is more favorable). Exploring this further would be an excellent topic for future work. Our simulations utilize ethanol (ε = 24.8520) as the implicit solvent, since it is representative of the range of dielectric constants of the hypothetical ESs. Further rationale for this choice is provided in ESI† Section S2.

The computational workflow is fully automated, thus enabling the quick generation of Gaussian16 input files, the collection and analysis of the energies, and the creation of the pathway energies. The workflow, which heavily utilizes the atomic simulation environment (ASE),[56] ensures that all potential binding sites are explored for each structure. For every structure presented in Fig. 1, the necessary reactions for each component presented in Table 1 are calculated. Free energies are estimated by adding the vibrational free energy contributions from the harmonic oscillator approximation to the electronic energies. The vibrational contributions are calculated using the pMuTT[57] python package. All vibrational frequencies below 50 cm^{-1} are set equal to 50 cm^{-1} to avoid overestimating the entropic contribution of low-frequency modes, which is a limitation of the harmonic oscillator approximation.[58] The energy of $[H]^+$ is calculated relative to H_3O^+/H_2O, *i.e.*, $G_{[H]^+} = G_{[H_3O]^+} - G_{H_2O}$, since it is not

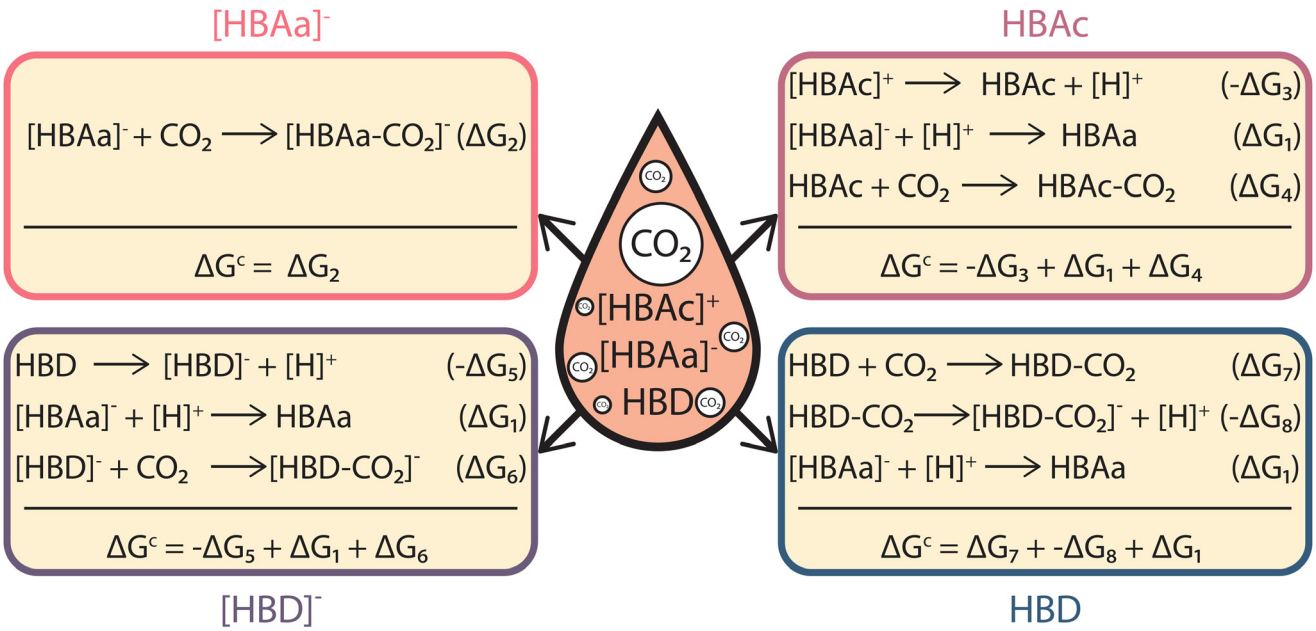

Fig. 3 The different CO_2 complexation pathways considered for a $[HBAc]^+[HBAa]^-$:HBD ES. Complexation occurs *via* the $[HBAa]^-$ (pink), HBAc (mauve), $[HBD]^-$ (purple), and HBD (blue) pathways. Reaction numbers are the same as in Table 1. Only the $[HBAa]^-$ pathway does not require a proton transfer for CO_2 complexation. The other three pathways all involve an intermolecular proton transfer, which is modeled here as occurring to the $[HBAa]^-$ species.

possible to compute the energy of an isolated proton ($G_{[H]^+}$) in most electronic structure software. This is a modeling choice that does not impact the results, but enables the calculation of relative proton transfer reaction free energies.

Results

CO_2 complexation

CO_2 complexation to the $[HBAa]^-$ species. The CO_2 binding free energies to the $[HBAa]^-$ species (which are equal to the complexation pathway free energies, ΔG^c; see Fig. 3) are plotted in Fig. 4. These values range from −14.7 kJ mol^{-1} to −94.9 kJ mol^{-1}. The species considered feature secondary amines and are organized by structural similarity in Fig. 4. For example, the different $[Im]^-$ species feature different functional groups (*i.e.*, R–H, R–CH_3, and R–CH_2-CH_3) anchored to the ring C atom between the two ring secondary amines (NR_2), and $[BIm]^-$ features a benzene ring anchored to the 5-membered ring. These functional groups induce minimal variations on the CO_2 complexation free energies, with values of ΔG^c ranging from −60 kJ mol^{-1} to −70 kJ mol^{-1}. The same can be said for the $[Trz]^-$ family as well as for $[Pyz]^-$ and $[Ind]^-$. In contrast, the $[Pyr]^-$ family has drastically different CO_2 complexation energies. Despite the same ring N binding site, $[Pyr]^-$ has a drastically different energy compared to $[2\text{-CNpyr}]^-$. Structurally, the difference between $[Pyr]^-$ and $[2\text{-CNpyr}]^-$ is a change in the functional group (R–H to R–CN) at the adjacent ring C site. The presence of the cyano group (R–CN) weakens the binding energy by ∼45 kJ mol^{-1}.

The influence of chemical functionality on CO_2 complexation is further investigated by systematically adding different functional groups around the CO_2 binding site on both the $[Pyr]^-$ and $[Im]^-$ species. The influence of different functional groups on CO_2 complexation free energies to [Pyr–

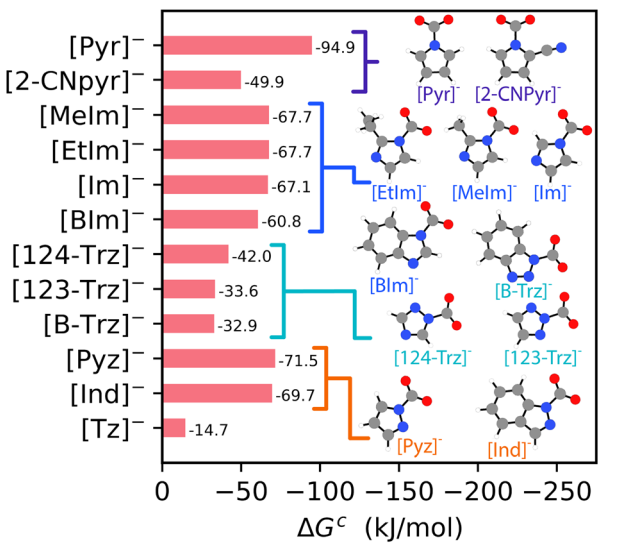

Fig. 4 The $[HBAa]^-$ CO_2 complexation free energies (in kJ mol^{-1}), where $\Delta G^c = \Delta G_2$. The figure is organized by structural similarity to compare how functionalization impacts CO_2 binding. Chemical structures are included to illustrate structural similarities and differences. Atom color key: gray = carbon, blue = nitrogen, red = oxygen, white = hydrogen. Different families of $[HBAa]^-$ species are denoted with the purple, blue, teal, and orange brackets.

$X]^-$ and $[Im–X]^-$ species, where X represents the different functional groups, is presented in Fig. 5. We find that alkyl functional groups (*i.e.*, R–Et and R–Me), which are considered weakly electron-donating groups, exhibit similar free energies as the parent $[Pyr]^-$ and $[Im]^-$ structures. The main electron donating groups considered are R–OH, R–MeOH, and R–EtOH. For $[Pyr–X]^-$, only R–OH results in stronger CO_2 complexation (by ~15 kJ mol^{-1}). In contrast, R–MeOH leads to a similar complexation energy, and R–EtOH has a CO_2 complexation energy that is less favorable (more positive) by ~11 kJ mol^{-1}. For $[Im–X]^-$, the presence of all electron donating groups leads to more negative (stronger) CO_2 complexation energies, ranging from ~12 to 20 kJ mol^{-1} compared to $[Im]^-$.

Conversely, the presence of electron withdrawing groups leads to more positive (*i.e.*, less thermodynamically favorable) CO_2 complexation energies compared to the parent species. Electron withdrawing groups remove electron density from the ring structure, resulting in a less nucleophilic N binding sites for CO_2 complexation. These results suggest that CO_2 complexation free energies to $[HBAa]^-$ species may be tuned with careful selection of the functional groups adjacent to the N binding site. In general, the CO_2 complexation results for the $[HBAa]^-$ species highlight the potential tunability of CO_2 complexation to the $[HBAa]^-$ species.

CO_2 complexation to the $[HBAc]^+$ species. Free energies involved in CO_2 complexation to the $[HBAc]^+$ species are presented in Fig. 6. Unlike for the $[HBAa]^-$ species, CO_2 complexation to the $[HBAc]^+$ species requires an intermolecular proton transfer, forming the HBAc species. The proton transfer from the $[HBAc]^+$ to the $[HBAa]^-$ occurs *via* the reverse of reaction R3 plus reaction R1, with free energy equal to $-\Delta G_3 + \Delta G_1$. These quantities are plotted in Fig. 6 with the orange bars using $[Im]^-$ as a reference. Selecting a different $[HBAa]^-$ would simply shift these free energies. A more negative proton transfer energy indicates that the $[HBAc]^+$ is more likely to donate a proton to $[Im]^-$. Both $[EMIM]^+$ and $[Ch]^+$ exhibit positive proton transfer free energies ($\Delta G_3 < \Delta G_1$), meaning that they are less likely to donate a proton to the $[Im]^-$ species. However, the sulfur-containing $[HBAc]^+$ species (*i.e.*, $[EMMTH]^+$, $[EHMTH]^+$, and $[ETH]^+$) all exhibit negative proton transfer free energies ($\Delta G_3 > \Delta G_1$), meaning that they are more likely to donate a proton to the $[Im]^-$ species. Furthermore,

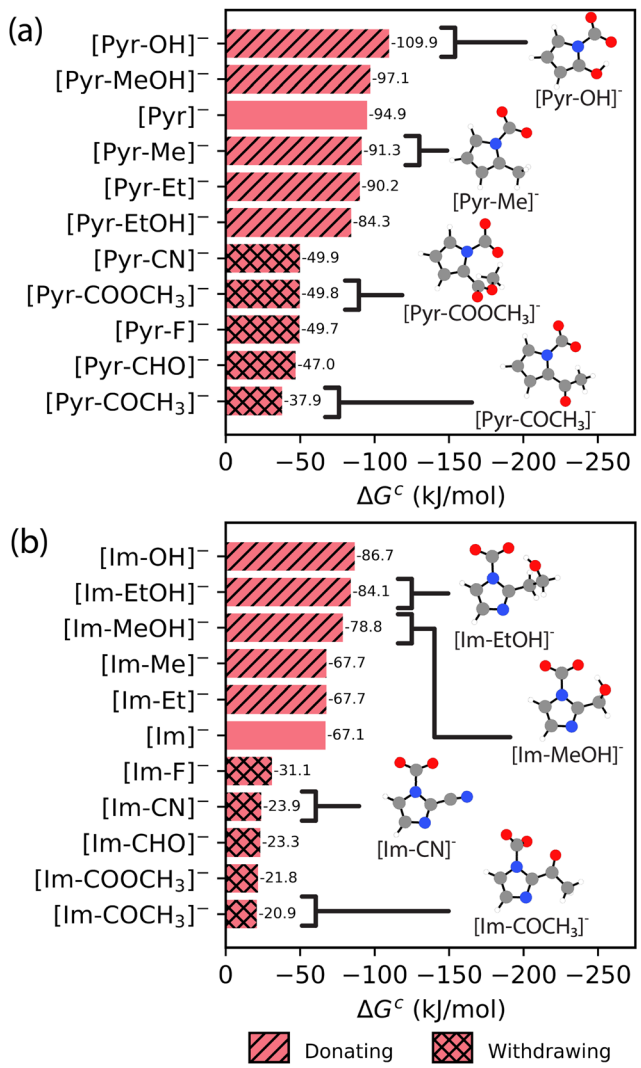

Fig. 5 The $[HBAa]^-$ CO_2 complexation free energies (in kJ mol^{-1}), where $\Delta G^c = \Delta G_2$ for the (a) $[Pyr–X]^-$ and (b) $[Im–X]^-$ families with different functional groups (as shown in Fig. 2). The single hatch indicates electron-donating groups and the double hatch indicates electron-withdrawing groups. The naming conventions for structures appearing in Fig. 4 are modified according to the naming convention in Fig. 2 (*i.e.*, $[Pyr–CN]^-$ = [2–CNpyr]$^-$, $[Im–Me]^-$ = [MeIm]$^-$, and $[Im–Et]^-$ = [EtIm]$^-$). Atom color key: gray = carbon, blue = nitrogen, red = oxygen, white = hydrogen.

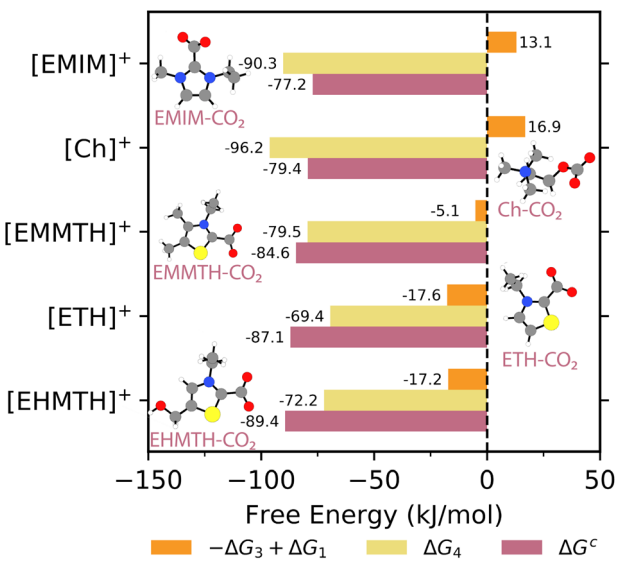

Fig. 6 The HBAc pathway free energies ($\Delta G^c = -\Delta G_3 + \Delta G_1 + \Delta G_4$; mauve), the proton transfer free energies ($-\Delta G_3 + \Delta G_1$; orange), and the CO_2 binding free energies (ΔG_4; yellow). ΔG_1 is calculated using $[Im]^-$ as the proton acceptor. The structure insets illustrate the CO_2 complexation final products. Atom color key: gray = carbon, blue = nitrogen, red = oxygen, white = hydrogen, yellow = sulfur.

these species exhibit small deviations in proton transfer free energies (−5.1 kJ mol^{-1} to −17.2 kJ mol^{-1}) as a function of the functional groups attached to the ring C atoms (*i.e.*, R–H, R–CH_2OH, and R–CH_3).

The overall CO_2 complexation pathway free energies (ΔG^c) for the $[HBAc]^+$ species are presented by the mauve bars in Fig. 6. The pathway free energies are obtained by summing the proton transfer free energies with the CO_2 binding energy, *i.e.*, $-\Delta G_3 + \Delta G_1 + \Delta G_4$. Overall, the CO_2 complexation pathway free energies range from −77.2 kJ mol^{-1} to −89.4 kJ mol^{-1}. They are strongly negative due to the favorable/negative CO_2 binding free energies (*i.e.*, ΔG_4), which span from −69.4 kJ mol^{-1} to −96.2 kJ mol^{-1} (yellow bars in Fig. 6). As previously mentioned, the sulfur-containing $[HBAc]^+$ species exhibit deviations in proton transfer energies. However, these deviations are not observed in the ΔG^c free energies (−84.6 kJ mol^{-1} to −89.4 kJ mol^{-1}). The CO_2 binding free energies (ΔG_4) compensate for the differences in proton transfer free energies for the $[EMMTH]^+$, $[EHMTH]^+$, and $[ETH]^+$ species, such that the overall complexation free energies for all $[HBAc]^+$ species are similar.

CO_2 complexation to the HBD species. The product for CO_2 complexation to the HBD species is $[HBD–CO_2]^-$, which involves CO_2 complexation onto the –N site (*e.g.*, PDA, TDA, and EDA) or the –OH site (*e.g.*, EG, PG, GOL). Two pathways leading to the same $[HBD–CO_2]^-$ products are considered. They are denoted by the initial step, which either forms a weakly complexed CO_2 (HBD–CO_2) or deprotonated HBD species ($[HBD]^-$). In the weak CO_2 complexation HBD pathway, CO_2 initially weakly complexes to the HBD (reaction R7) before proton transfer to the $[HBAa]^-$ (reverse of reaction R8 plus reaction R1). For the deprotonated HBD pathway, the proton transfer to the $[HBAa]^-$ (reverse of reaction R5 plus reaction R1) occurs first, forming an $[HBD]^-$ species. CO_2 then complexes to the $[HBD]^-$ species (reaction R6). Both pathways are considered to investigate the differences in the thermodynamic landscape, even though the final values of ΔG^c are the same.

Free energies involved in CO_2 complexation to the different HBD species are reported in Fig. 7. Overall, the CO_2 complexation pathways for the different HBD species (green bars in Fig. 7) are thermodynamically similar, with ΔG^c of ∼−65 kJ mol^{-1}, despite variations in the chain length of the diamine species (increasing in length from EDA to TDA to PDA). The exception is GOL, which forms an intramolecular hydrogen bond between the complexed CO_2 and the adjacent –OH group and exhibits ΔG^c of −87.5 kJ mol^{-1}, but even this difference is minor. All HBDs considered in this work prefer the pathway where weak CO_2 complexation occurs initially. This is due to the proton transfer free energies being more favorable from the weakly complexed species than for the uncomplexed species (*i.e.*, $-\Delta G_5 + \Delta G_1 \gg \Delta G_7$; more positive purple bars than blue bars in Fig. 7). This is particularly true for the HBDs with the –N site, where proton transfer from the HBD is

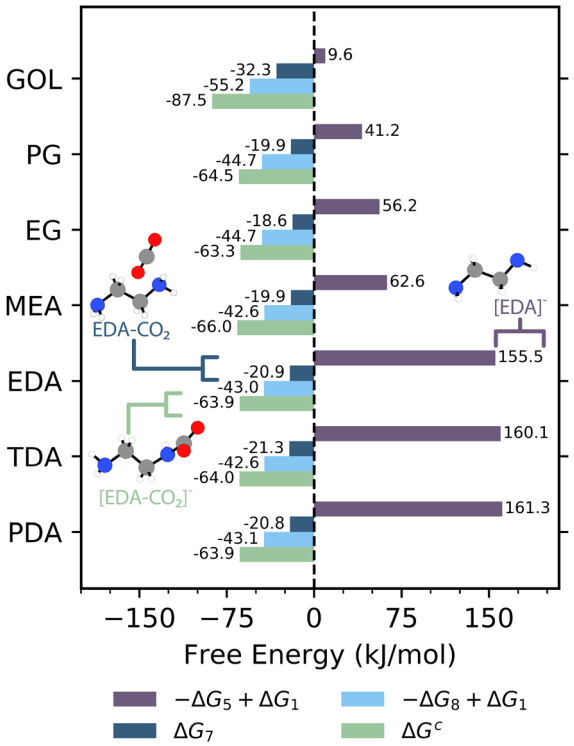

Fig. 7 The HBD/$[HBD]^-$ CO_2 complexation pathway free energies ($\Delta G^c = -\Delta G_5 + \Delta G_1 + \Delta G_6 = \Delta G_7 - \Delta G_8 + \Delta G_1$; green), the free energies for transferring a proton from the HBD to $[Im]^-$ ($-\Delta G_5 + \Delta G_1$; purple), the free energy of weak CO_2 complexation (ΔG_7; blue), and the free energies of proton transfer from HBD–CO_2 to $[Im]^-$ ($-\Delta G_8 + \Delta G_1$; light blue). ΔG_1 is calculated using $[Im]^-$ as the proton acceptor. The structure inserts demonstrate the different intermediates for the HBD and $[HBD]^-$ complexation pathways. Atom color key: gray = carbon, blue = nitrogen, red = oxygen, white = hydrogen.

significantly uphill (∼160 kJ mol^{-1}) compared to the free energy to form HBD–CO_2 species (∼−20 kJ mol^{-1}), and because the free energies of proton transfer from the weakly complexed HBD–CO_2 species (*i.e.*, $-\Delta G_8 + \Delta G_1$) are negative for all HBD species.

Comparing CO_2 complexation pathways. As previously discussed, the complexation pathways to the $[HBAc]^+$ and HBD species involve multiple steps. To understand which species CO_2 is more likely to bind to, proton transfer free energies for the $[HBAc]^+$ species are compared to weak CO_2 complexation of the HBD pathway in Fig. 8a. Additional comparisons between the proton transfer steps for the $[HBD]^-$ and HBAc pathways are presented in Fig. S6.† Specifically, Fig. 8a plots the difference in the weak complexation CO_2 free energies (ΔG_7) and the proton transfer free energies ($-\Delta G_3 + \Delta G_1$), with values ranging from ∼0 kJ mol^{-1} to −49.2 kJ mol^{-1}. All values are negative. For $[Ch]^+$ and $[EMIM]^+$, the free energy differences range from ∼−30 kJ mol^{-1} to ∼−50 kJ mol^{-1}, demonstrating that weak CO_2 complexation to the HBD species is preferred. That said, $[EHMTH]^+$ and $[ETH]^+$ exhibit free energies that are ∼0 kJ mol^{-1}, suggesting that HBD–CO_2 and HBAc species are both likely to occur in solution.

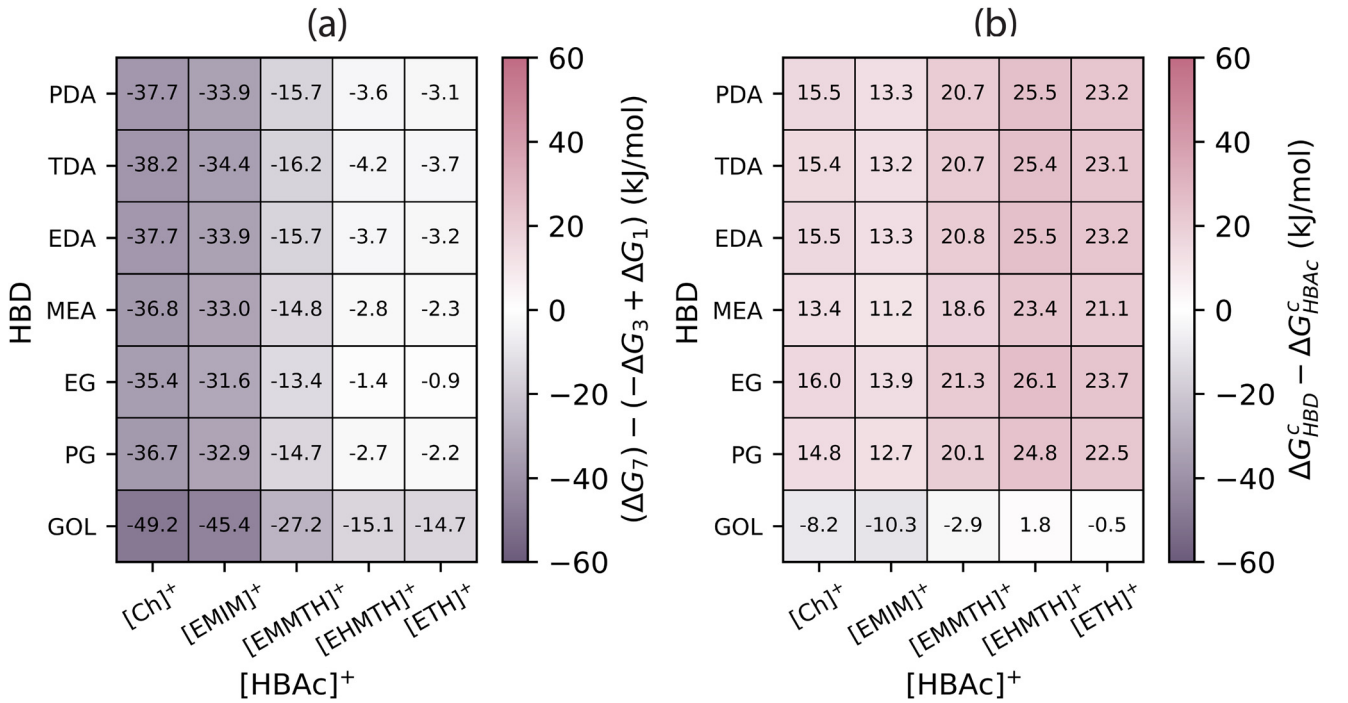

Fig. 8 Heat maps comparing the free energies between the HBD and HBAc pathways: (a) difference between the weakly complexed CO_2 step (ΔG_7) and the proton transfer step ($-\Delta G_3 + \Delta G_1$) free energies and (b) difference between HBD (ΔG^c_{HBD}) and HBAc $\left(\Delta G^c_{[HBAa]^+}\right)$ complexation pathway free energies. For the proton transfer steps, the energy (ΔG_1) is calculated using $[Im]^-$ as the proton acceptor. The color bar indicates the more favorable pathway. For (a), purple indicates that weak complex is more favorable ($\Delta G_7 < -\Delta G_3 + \Delta G_1$) and mauve indicates the proton transfer is more favorable ($\Delta G_7 > -\Delta G_3 + \Delta G_1$). For (b), purple indicates that the HBD complexation is preferred ($\Delta G^c_{HBD} < \Delta G^c_{HBAc}$) and mauve indicates that the HBAc complexation pathway is preferred ($\Delta G^c_{HBD} > \Delta G^c_{HBAc}$).

The HBD *vs.* $[HBAc]^+$ pathway complexation free energies $\left(\Delta G^c_{HBD}\ vs.\ \Delta G^c_{[HBAc]^+}\right)$ are presented in Fig. 8b. Specifically, Fig. 8b plots the difference between the HBD complexation pathway (ΔG^c_{HBD}) and the HBAc complexation pathway (ΔG^c_{HBAc}) free energies. For all species except GOL, the reported free energies differences are positive ($\Delta G^c_{HBD} - \Delta G^c_{HBAc} > 0$), with free energies ranging from ~11 kJ mol^{-1} to ~26 kJ mol^{-1}. These results indicate that for all HBD species except GOL, CO_2 complexation to the HBAc is favored (*i.e.*, $\Delta G^c_{HBAc} < \Delta G^c_{HBD}$).

The free energies for the $[HBAa]^-$ and HBD complexation pathways are compared in Fig. 9. Since the $[HBAa]^-$ does not require proton transfer, the free energy of CO_2 binding to the $[HBAa]^-$ species (ΔG_2) is compared to the free energy of weak CO_2 complexation to the HBD (ΔG_7) in Fig. 9a. The difference in free energies ranges from −18 kJ mol^{-1} to +76 kJ mol^{-1}. These differences are strongly influenced by the $[HBAa]^-$ species, which exhibits large variations in CO_2 complexation free energies (ΔG_2) as reported in Fig. 4. However, the overall complexation pathway free energies are presented in Fig. 9b and show a more neutral thermodynamic landscape $\left(i.e.,\ \Delta G^c_{HBD} - \Delta G^c_{[HBAa]^-} \approx 0\right)$ for most $[HBAa]^-$/HBD pairs with only GOL breaking this trend. Overall, this suggests that thermodynamically, these species are approximately equally likely to complex CO_2.

Discussion

The values of ΔG^c calculated in this work support that, with the exception of GOL, CO_2 complexation to the $[HBAc]^+$ is favored, but that multiple complexation pathways are present within eutectic solvents, with CO_2 complexation occurring to the $[HBAc]^+$, $[HBAa]^-$, and HBD species. This suggests that multiple CO_2 sorption products could be present in IL/ES/DES solvents. This poses significant challenges when designing different sorbents with specific CO_2 uptake properties since identifying the mechanisms and thermodynamics for complexation is challenging. Although not explored here, understanding CO_2 complexation is also further complicated by a single species potentially complexing multiple CO_2. For example, while our structure library only considers a single CO_2 complexation for each HBD, experimentally, certain HBD species have been observed to complex multiple CO_2 molecules.[10,59] When rationalizing experimental uptake data, understanding the locations and potential for a single species that complexes multiple CO_2 molecules is important to identify the different mechanisms.

Furthermore, our findings demonstrate that functional groups around the complexation site result in large deviations (~70 kJ mol^{-1}) of the CO_2 complexation energies. The electron-donating groups display more favorable (*i.e.*, more negative values of ΔG^c); electron-withdrawing groups

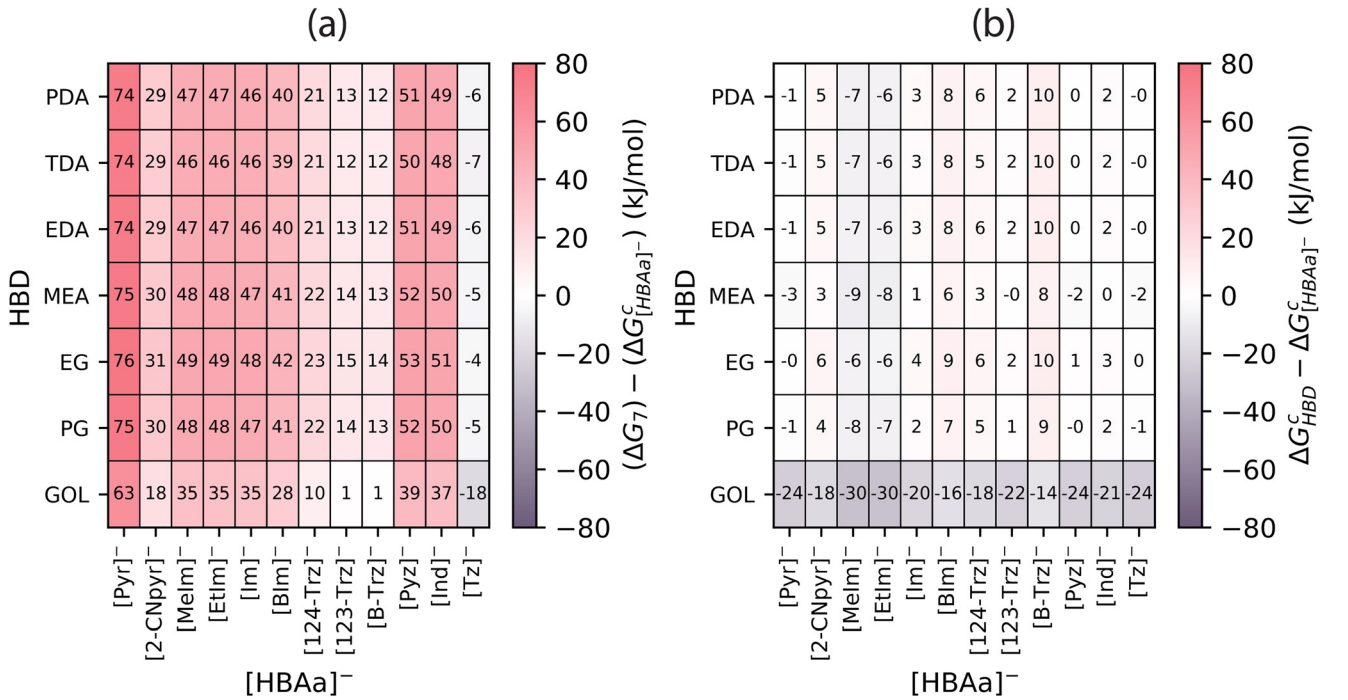

Fig. 9 Heat maps comparing the free energies between the HBD and $[HBAa]^-$ pathways: (a) difference between the weak CO_2 complexation free energy (ΔG_7) and the $[HBAa]^-$ CO_2 complexation free energy (ΔG_2) and (b) difference between HBD (ΔG^c_{HBD}) and $[HBAa]^-$ $\left(\Delta G^c_{[HBAa]^-}\right)$ complexation pathway free energies. For the proton transfer steps, the energy (ΔG_1) is calculated using the corresponding $[HBAa]^-$ species as the proton acceptor. The color bar indicates the more favorable pathway. For (a), purple indicates that weak complexation to the HBD is more favorable ($\Delta G_7 < \Delta G_2$) and pink indicates that complexation to the $[HBAa]^-$ is more favorable ($\Delta G_7 > \Delta G_2$). For (b), purple indicates that the HBD complexation pathway is preferred $\left(\Delta G^c_{HBD} < \Delta G^c_{[HBAa]^-}\right)$ and pink indicates that the $[HBAa]^-$ complexation pathway is preferred $\left(\Delta G^c_{HBD} > \Delta G^c_{[HBAa]^-}\right)$.

display less favorable (*i.e.*, more positive values of ΔG^c). Generally, the species with more negative complexation free energies display intramolecular hydrogen bonds between the complexed CO_2 and adjacent ligands. As reported in Fig. S7,† these intramolecular hydrogen bonds lower the CO_2 complexation free energies by ~30 kJ mol^{-1} for the [IM–EtOH]$^-$, [IM–MeOH]$^-$, and [Pyr–OH]$^-$ species. This observation supports the observation made by Klemm *et al.* that intramolecular hydrogen bond formation stabilizes complexed CO_2 reaction intermediates.[14] Overall, these findings suggest that rationally selecting the functional groups around the CO_2 binding site provides significant opportunities for tuning CO_2 complexation.

Another potential mechanism for tuning CO_2 complexation is considering the nucleophilicity of a given molecule, which is well established for CO_2 complexation.[60] Most CO_2 sorption materials rely on nucleophiles (*i.e.*, containing electron lone pairs) to capture CO_2. However, the same strong, electron-rich character also promotes proton transfer reactions. The relationship between nucleophilicity to both CO_2 binding and proton transfer reactions presents a challenge in designing solvents (Fig. S8 and S9†). For the $[HBAa]^-$ species (Fig. S9a†), a more negative (*i.e.*, stronger) proton transfer free energy indicates a more negative (*i.e.*, stronger) CO_2 binding energy, and this is attributed to the increased nucleophilicity of the $[HBAa]^-$. A similar observation is established for both $[HBAc]^+$ (Fig. S9b†) and $[HBD]^-$ species (Fig. S8†). However, since the HBAc and $[HBD]^-$ rely on intermolecular proton transfers for CO_2 complexation, a stronger (more negative) proton transfer energy leads to unfavorable CO_2 binding thermodynamics as these species must donate a proton. These findings support the idea that there is a competitive process between CO_2 binding and proton affinity for an $[HBAa]^-$ species, which can be attributed to the nucleophilicity of the species. The interplay between nucleophilicity and the CO_2 binding and proton transfer steps is fundamental to the CO_2 complexation process. A strong correlation between the CO_2 binding and proton transfer reactions for all $[HBAc]^+$, $[HBAa]^-$ and HBD species suggests that experimental parameters (*i.e.*, proton affinity or pK_a)[61] might be a reasonable descriptor for CO_2 binding.

Additionally, the hydrogen bond network[62–64] within ILs and DESs/ESs poses further challenges in understanding CO_2 complexation. In ILs, the hydrogen bond network is relatively simple, with hydrogen bonds forming between the $[HBAc]^+$ and $[HBAa]^-$.[65,66] The inclusion of the HBD complicates the hydrogen bond network by adding additional hydrogen bond interactions ($[HBAc]^+/[HBAa]^-$, $[HBAa]^-$/HBD, and $[HBAa]^-$/HBD).[67,68] The hydrogen bond network can have a significant influence on how and where CO_2 complexation occurs.[14,39,69,70] Tuning CO_2 complexation *via* the rational

selection of HBDs is another potential 'design' variable outside the scope of this particular work.

Overall, our findings demonstrate a large range of complexation free energies to the different ILs/DESs/ESs components. Prior literature suggests reaction enthalpies ranging from ~−50 kJ mol^{-1} to −65 kJ mol^{-1} for energy-efficient DAC.[71,72] Using this range of values as a guide, systems consisting of imidazolide (*i.e.*, $[Im]^-$, $[MeIm]^-$, $[EtIm]^-$, and $[BIm]^-$) and 2-cyanopyrrolide ($[2\text{-}CNpyr]^-$) as $[HBAa]^-$ species and all HBD species considered exhibit complexation free energies within the target range. These findings are supported by experimental observations in reaction enthalpies for an $[EMIM]^+[2\text{-}CNpyr]^-$ IL[73] and potential production distribution for an $[MEAH]^+[Im]^-$:EG DES.[74] Elucidating the thermodynamic landscape by investigating the CO_2 complexation is a necessary first step towards designing DAC materials but cannot fully explain CO_2 sorption. Additional information about mass transfer[75] and reaction kinetics[76] and mechanisms would be needed to fully clarify CO_2 uptake. Such investigations would be good topics for future work.

Conclusion

DFT calculations provide insights into the thermodynamics for CO_2 complexation to hypothetical ESs ($[HBAc]^+[HBAa]^-$:HBD). A structure library, comprised of different $[HBAc]^+$, $[HBAa]^-$, and HBD species is used to model CO_2 binding and proton transfer reaction steps, given that these fundamental reactions are involved in CO_2 complexation. The $[HBAa]^-$ complexation pathway is the simplest since no intermolecular proton transfer is required for CO_2 binding. However, both the $[HBAc]^+$ and the HBD species require an intermolecular proton transfer for CO_2 complexation. The complexation thermodynamics behind these pathways are explored, with the HBAc pathway being slightly more thermodynamically favorable compared to the $[HBAa]^-$ and HBD pathways. However, differences in the experimentally, observed product distributions could be influenced by free energy effects related to solvent structure that are beyond the scope of this work.

Furthermore, the functional groups surrounding the CO_2 binding site influence on complexation is also studied for the $[HBAa]^-$ species and $[HBAc]^+$ species. For $[HBAa]^-$, the N binding site is 'tuned' by electron-withdrawing and electron-donating groups near the binding site. The findings demonstrate that electron-withdrawing groups lead to weaker (less favorable) complexation free energies, whereas electron-donating groups lead to stronger (more favorable) complexation free energies. For $[HBAc]^+$, deviations for the $[ETH]^+$-based species (*i.e.*, different functional groups R–H, R –CH_2OH, and R–CH_3) is observed. Interestingly, these findings suggest that there might be differences in the functional groups that impact complexation to the $[HBAc]^+$ and $[HBAa]^-$ species. Our findings suggest that tuning CO_2 complexation *via* functionalization is possible.

Data availability

The data supporting this article have been included as part of the ESI.† Additionally, all structures are located on a GitHub repository.

Author contributions

SPV designed the study, performed the calculations, analyzed the data, wrote the initial manuscript draft, and reviewed and edited the manuscript. OI performed calculations and reviewed and edited the manuscript. RBG designed the study, supervised the work, reviewed and edited the manuscript, and provided financial support.

Conflicts of interest

The authors declare no competing interests.

Acknowledgements

This work is supported by the U.S. Department of Energy, Office of Science, Basic Energy Sciences under award number DESC0022214. SPV was also supported by a GAANN Fellowship (Award Number: P200A180076) from the United States Department of Education. SPV and RBG would like to acknowledge the Clemson Computing and Information Technology (CITI) Advanced Computing and Data Science (ACDS) group for the generous allotment of compute time on the Palmetto cluster. OI and RBG would also like to thank the Ohio Supercomputer Center for its high-performance computing resources and expertise.

Notes and references

1 T. Stocker, Q. Dahe, G. Plattner, M. Tignor, S. Allen, J. Boschung, A. Nauels, Y. Xia, V. Bex and P. Midgley, The Intergovernmental Panel on Climate Change (IPCC) 2013: Summary for Policymakers, in *Climate Change 2013: The Physical Science Basis, Contribution of Working Group I to the Fifth Assessment Report of the Intergovernmental Panel on Climate Change*, 2013.
2 D. McLaren, *Process Saf. Environ. Prot.*, 2012, **90**, 489–500.
3 N. A. of Sciences Engineering and Medicine, *Negative Emissions Technologies and Reliable Sequestration: A Research Agenda*, National Academies Press, 2019, pp. 1–510.
4 J. Rosen, *Science*, 2018, **359**, 733–737.
5 G. Iyer, L. Clarke, J. Edmonds, A. Fawcett, J. Fuhrman, H. McJeon and S. Waldhoff, *Energy Clim. Change*, 2021, **2**, 1–5.
6 I. P. on Climate Change (IPCC), in *Summary for Policymakers*, Cambridge University Press, 2022, pp. 1–24.
7 Y. Qiu, P. Lamers, V. Daioglou, N. McQueen, H. S. de Boer, M. Harmsen, J. Wilcox, A. Bardow and S. Suh, *Nat. Commun.*, 2022, **13**, 1–13.
8 J. F. Wiegner, A. Grimm, L. Weimann and M. Gazzani, *Ind. Eng. Chem. Res.*, 2022, 12649–12667.
9 G. Li and J. Yao, *Engineering*, 2024, **5**, 1298–1336.

10 R. Dikki, E. Cagli, D. Penley, M. Karayilan and B. Gurkan, *Chem. Commun.*, 2023, 12027–12030.
11 K. E. Gutowski and E. J. Maginn, *J. Am. Chem. Soc.*, 2008, **130**, 14690–14704.
12 B. Peric, J. Sierra, E. Martí, R. Cruañas, M. A. Garau, J. Arning, U. Bottin-Weber and S. Stolte, *J. Hazard. Mater.*, 2013, **261**, 99–105.
13 M. Chen and J. Xu, *Molecules*, 2023, **28**, 1–10.
14 A. Klemm, S. P. Vicchio, S. Bhattacharjee, E. Cagli, Y. Park, M. Zeeshan, R. Dikki, H. Liu, M. K. Kidder, R. B. Getman and B. Gurkan, *ACS Sustainable Chem. Eng.*, 2023, **11**, 3740–3749.
15 V. Migliorati, F. Sessa and P. D'Angelo, *Chem. Phys. Lett.*, 2019, **2**, 1–7.
16 C. A. Trickett, A. Helal, B. A. Al-Maythalony, Z. H. Yamani, K. E. Cordova and O. M. Yaghi, *Nat. Rev. Mater.*, 2017, **2**, 1–16.
17 S. Bose, D. Sengupta, T. M. Rayder, X. Wang, K. O. Kirlikovali, A. K. Sekizkardes, T. Islamoglu and O. K. Farha, *Adv. Funct. Mater.*, 2023, 1–19.
18 I. B. Orhan, T. C. Le, R. Babarao and A. W. Thornton, *Commun. Chem.*, 2023, **6**, 1–12.
19 A. Sinha, L. A. Darunte, C. W. Jones, M. J. Realff and Y. Kawajiri, *Ind. Eng. Chem. Res.*, 2017, **56**, 750–764.
20 L. Li, Z. Xiao, C. Xu, Y. Zhou and Z. Li, *Environ. Res.*, 2024, **262**, 1–10.
21 H. Lyu, H. Li, N. Hanikel, K. Wang and O. M. Yaghi, *J. Am. Chem. Soc.*, 2022, **144**, 12989–12995.
22 H. Li, A. Dilipkumar, S. Abubakar and D. Zhao, *Chem. Soc. Rev.*, 2023, **52**, 6294–6329.
23 Y. Zeng, R. Zou and Y. Zhao, *Adv. Mater.*, 2016, **28**, 2855–2873.
24 M. Zanatta, *ACS Mater. Au*, 2023, **3**, 576–583.
25 L. Lombardo, H. Yang, K. Zhao, P. J. Dyson and A. Züttel, *ChemSusChem*, 2020, **13**, 2025–2031.
26 W. R. Lee, S. Y. Hwang, D. W. Ryu, K. S. Lim, S. S. Han, D. Moon, J. Choi and C. S. Hong, *Energy Environ. Sci.*, 2014, **7**, 744–751.
27 S. Zeng, X. Zhang, L. Bai, X. Zhang, H. Wang, J. Wang, D. Bao, M. Li, X. Liu and S. Zhang, *Chem. Rev.*, 2017, **117**, 9625–9673.
28 J. Zhang, J. Sun, X. Zhang, Y. Zhao and S. Zhang, *Greenhouse Gases:Sci. Technol.*, 2011, **1**, 142–159.
29 X. Zhang, X. Zhang, H. Dong, Z. Zhao, S. Zhang and Y. Huang, *Energy Environ. Sci.*, 2012, **5**, 6668–6681.
30 Y. Gu, Y. Hou, S. Ren, Y. Sun and W. Wu, *ACS Omega*, 2020, **5**, 6809–6816.
31 N. V. Plechkova and K. R. Seddon, *Chem. Soc. Rev.*, 2008, **37**, 123–150.
32 R. Hayes, G. G. Warr and R. Atkin, *Chem. Rev.*, 2015, **115**, 6357–6426.
33 A. P. Abbott, G. Capper, D. L. Davies, R. K. Rasheed and V. Tambyrajah, *Chem. Commun.*, 2003, 70–71.
34 L. J. Kollau, M. Vis, A. V. D. Bruinhorst, A. C. C. Esteves and R. Tuinier, *Chem. Commun.*, 2018, **54**, 13351–13354.
35 N. F. Gajardo-Parra, V. P. Cotroneo-Figueroa, P. Aravena, V. Vesovic and R. I. Canales, *J. Chem. Eng. Data*, 2020, **65**, 5581–5592.
36 B. E. Gurkan, J. C. D. L. Fuente, E. M. Mindrup, L. E. Ficke, B. F. Goodrich, E. A. Price, W. F. Schneider and J. F. Brennecke, *J. Am. Chem. Soc.*, 2010, **132**, 2116–2117.
37 G. Latini, M. Signorile, V. Crocellà, S. Bocchini, C. F. Pirri and S. Bordiga, *Catal. Today*, 2019, **336**, 148–160.
38 M. Pan, Y. Zhao, X. Zeng and J. Zou, *Energy Fuels*, 2018, **32**, 6130–6135.
39 M. Chen, S. Zhang, Q. Mei, H. Zhou and D. Yang, *Chem. Commun.*, 2025, 1–4.
40 S. Oh, O. Morales-Collazo and J. F. Brennecke, *J. Phys. Chem. B*, 2019, **123**, 8274–8284.
41 S. Seo, M. A. Desilva and J. F. Brennecke, *J. Phys. Chem. B*, 2014, **118**, 14870–14879.
42 B. Yoon, S. Chen and G. A. Voth, *J. Am. Chem. Soc.*, 2024, **146**, 1612–1618.
43 W. Kong, X. Zhong, K. Yang, Z. Dong, T. Song, M. Fang, T. Wang, S. Zhang, W. Li and S. Li, *Chem. Eng. J.*, 2025, **504**, 1–15.
44 J. Ma, Y. Du, M. Liu, Y. Zhou, X. Wang, B. Wang, J. Zhu and M. Zhu, *J. Phys. Chem. B*, 2024, 372–384.
45 A. Al-Bodour, N. Alomari, S. Aparicio and M. Atilhan, *J. Mol. Liq.*, 2023, **390**, 1–13.
46 B. Yoon and G. A. Voth, *J. Am. Chem. Soc.*, 2023, **145**, 15663–15667.
47 Y. Y. Lee, D. Penley, A. Klemm, W. Dean and B. Gurkan, *ACS Sustainable Chem. Eng.*, 2021, **9**, 1090–1098.
48 X. Li, M. Hou, Z. Zhang, B. Han, G. Yang, X. Wang and L. Zou, *Green Chem.*, 2008, **10**, 879–888.
49 S. Onofri and E. Bodo, *J. Phys. Chem. B*, 2021, **125**, 5611–5619.
50 W. T. Zheng, K. Huang, Y. T. Wu and X. B. Hu, *AIChE J.*, 2018, **64**, 209–219.
51 B. Li, Y. Fu, Z. Yang, S. Dai and D. E. Jiang, *J. Phys. Chem. B*, 2024, 10207–10213.
52 DAC-Screening-Data-Repository, 2025, **https://github.com/getman-research-group/DAC_Screening_Data_Repository**, [Online; accessed 2025-02-22].
53 M. J. Frisch, G. W. Trucks, H. B. Schlegel, G. E. Scuseria, M. A. Robb, J. R. Cheeseman, G. Scalmani, V. Barone, G. A. Petersson, H. Nakatsuji, X. Li, M. Caricato, A. V. Marenich, J. Bloino, B. G. Janesko, R. Gomperts, B. Mennucci, H. P. Hratchian, J. V. Ortiz, A. F. Izmaylov, J. L. Sonnenberg, D. Williams-Young, F. Ding, F. Lipparini, F. Egidi, J. Goings, B. Peng, A. Petrone, T. Henderson, D. Ranasinghe, V. G. Zakrzewski, J. Gao, N. Rega, G. Zheng, W. Liang, M. Hada, M. Ehara, K. Toyota, R. Fukuda, J. Hasegawa, M. Ishida, T. Nakajima, Y. Honda, O. Kitao, H. Nakai, T. Vreven, K. Throssell, J. A. Montgomery Jr , J. E. Peralta, F. Ogliaro, M. J. Bearpark, J. J. Heyd, E. N. Brothers, K. N. Kudin, V. N. Staroverov, T. A. Keith, R. Kobayashi, J. Normand, K. Raghavachari, A. P. Rendell, J. C. Burant, S. S. Iyengar, J. Tomasi, M. Cossi, J. M. Millam, M. Klene, C. Adamo, R. Cammi, J. W. Ochterski, R. L. Martin, K. Morokuma, O. Farkas, J. B. Foresman and D. J. Fox, *Gaussian16 Revision C.02*, Gaussian Inc., Wallingford CT, 2016.
54 S. Grimme, W. Hujo and B. Kirchner, *Phys. Chem. Chem. Phys.*, 2012, **14**, 4875–4883.

55 S. Grimme, S. Ehrlich and L. Goerigk, *J. Comput. Chem.*, 2011, **32**, 1456–1465.
56 A. H. Larsen, J. J. Mortensen, J. Blomqvist, I. E. Castelli, R. Christensen, M. Dułak, J. Friis, M. N. Groves, B. Hammer, C. Hargus, E. D. Hermes, P. C. Jennings, P. B. Jensen, J. Kermode, J. R. Kitchin, E. L. Kolsbjerg, J. Kubal, K. Kaasbjerg, S. Lysgaard, J. B. Maronsson, T. Maxson, T. Olsen, L. Pastewka, A. Peterson, C. Rostgaard, J. Schiøtz, O. Schütt, M. Strange, K. S. Thygesen, T. Vegge, L. Vilhelmsen, M. Walter, Z. Zeng and K. W. Jacobsen, *J. Phys.: Condens. Matter*, 2017, **29**, 1–31.
57 J. Lym, G. R. Wittreich and D. G. Vlachos, *Comput. Phys. Commun.*, 2019, 106864.
58 R. F. Ribeiro, A. V. Marenich, C. J. Cramer and D. G. Truhlar, *J. Phys. Chem. B*, 2011, **115**, 14556–14562.
59 X. Wu, J. Ruan, K. Wang, X. Zhang, M. Ma, L. Chen and Z. Qi, *Green Chem. Eng.*, 2024, 1–13.
60 J. H. Rheinhardt, P. Singh, P. Tarakeshwar and D. A. Buttry, *ACS Energy Lett.*, 2017, **2**, 454–461.
61 I. M. Bernhardsen, I. R. Krokvik, C. Perinu, D. D. Pinto, K. J. Jens and H. K. Knuutila, *Int. J. Greenhouse Gas Control*, 2018, **68**, 68–76.
62 P. A. Hunt, C. R. Ashworth and R. P. Matthews, *Chem. Soc. Rev.*, 2015, **44**, 1257–1288.
63 U. L. Abbas, Q. Qiao, M. T. Nguyen, J. Shi and Q. Shao, *AIChE J.*, 2022, **68**, 1–15.
64 D. K. Panda and B. L. Bhargava, *J. Mol. Graphics Modell.*, 2022, **113**, 1–9.
65 K. Dong and S. Zhang, *Chem. – Eur. J.*, 2012, **18**, 2748–2761.
66 S. Bhattacharjee, R. Dikki, B. Gurkan and R. B. Getman, *J. Mol. Liq.*, 2024, **410**, 125569.
67 R. Stefanovic, M. Ludwig, G. B. Webber, R. Atkin and A. J. Page, *Phys. Chem. Chem. Phys.*, 2017, **19**, 3297–3306.
68 Y. Zhang, D. Poe, L. Heroux, H. Squire, B. W. Doherty, Z. Long, M. Dadmun, B. Gurkan, M. E. Tuckerman and E. J. Maginn, *J. Phys. Chem. B*, 2020, **124**, 5251–5264.
69 C. Zhu, H. Wood, P. Carbone, C. D'Agostino and S. P. de Visser, *Phys. Chem. Chem. Phys.*, 2025, 2381–2394.
70 Z. Wang, M. Chen, B. Lu, S. Zhang and D. Yang, *ACS Sustainable Chem. Eng.*, 2023, **11**, 6272–6279.
71 Z. Yang and S. Dai, *Green Chem. Eng.*, 2021, **2**, 342–345.
72 R. P. Lively and M. J. Realff, *AIChE J.*, 2016, **62**, 3699–3705.
73 Y. Y. Lee, K. Edgehouse, A. Klemm, H. Mao, E. Pentzer and B. Gurkan, *ACS Appl. Mater. Interfaces*, 2020, **12**, 19184–19193.
74 J. Cheng, C. Wu, W. Gao, H. Li, Y. Ma, S. Liu and D. Yang, *Int. J. Mol. Sci.*, 2022, **23**, 1–7.
75 M. H. Abdellah, A. Kiani, W. Conway, G. Puxty and P. Feron, *Chem. Eng. J.*, 2024, **481**, 1–13.
76 M. Zanatta, N. M. Simon, F. P. dos Santos, M. C. Corvo, E. J. Cabrita and J. Dupont, *Angew. Chem., Int. Ed.*, 2019, **58**, 382–385.